Biological and Medical Applications of Materials and Interfaces

The impact of biomimicry in the design of osteoinductive bone substitutes: nanoscale matters

Albert Barba, Anna Diez-Escudero, Montserrat Espanol, Mar Bonany, Joanna Maria Sadowska, Jordi Guillem-Marti, Caroline Öhman-Mägi, Cecilia Persson, Maria-Cristina Manzanares, Jordi Franch, and Maria-Pau Ginebra

ACS Appl. Mater. Interfaces, **Just Accepted Manuscript** • DOI: 10.1021/acsami.8b20749 • Publication Date (Web): 11 Feb 2019

The impact of biomimicry in the design of osteoinductive bone substitutes: nanoscale matters

Albert Barba[a,b,c], Anna Diez-Escudero[a,b], Montserrat Espanol[a,b], Mar Bonany[a,b], Joanna Maria Sadowska[a,b], Jordi Guillem-Marti[a,b], Caroline Öhman-Mägi[d], Cecilia Persson[d], Maria-Cristina Manzanares[e], Jordi Franch[c], Maria-Pau Ginebra[a,b,f*]

[a]Biomaterials, Biomechanics and Tissue Engineering Group, Department of Materials Science and Metallurgical Engineering, Universitat Politècnica de Catalunya, Av. Eduard Maristany 10-14, 08019 Barcelona, Spain

[b]Barcelona Research Center in Multiscale Science and Engineering, Universitat Politècnica de Catalunya, Av. Eduard Maristany 10-14, 08019 Barcelona, Spain

[c]Bone Healing Group, Small Animal Surgery Department, Veterinary School, Universitat Autònoma de Barcelona, 08193 Bellaterra (Barcelona), Spain

[d]Materials in Medicine Group, Division of Applied Materials Science, Department of Engineering Sciences, Uppsala University, 751 21 Uppsala, Sweden

[e]Human Anatomy and Embryology Unit, Department of Pathology and Experimental Therapeutics, Universitat de Barcelona, 08907 L'Hospitalet de Llobregat (Barcelona), Spain

[f]Institut for Bioengineering of Catalonia (IBEC), Barcelona Institute of Technology (BIST), 08028 Barcelona, Spain

* Corresponding author: maria.pau.ginebra@upc.edu

Keywords: biomimetic; calcium phosphate; carbonated apatite; nanostructure; foaming; osteoinduction; osteogenesis

Abstract

Bone apatite consists in carbonated calcium deficient hydroxyapatite nanocrystals (CDHA). Biomimetic routes allow fabricating synthetic bone grafts that mimic biological apatite. In this work, we explored the role of two distinctive features of biomimetic apatites, namely nanocrystal morphology (plate *vs.* needle-like crystals) and carbonate content on the bone regeneration potential of CDHA scaffolds in an *in vivo* canine model. Both ectopic bone formation and scaffold degradation were drastically affected by the nanocrystal morphology after intramuscular implantation. Fine-CDHA foams with needle-like nanocrystals, comparable in size to bone mineral, showed a markedly higher osteoinductive potential and a superior degradation than chemically identical Coarse-CDHA foams with larger plate-shaped crystals. These findings correlated well with the superior bone healing capacity showed by the Fine-CDHA scaffolds when implanted intraosseously. Moreover, carbonate doping of CDHA, which resulted in small plate-shaped nanocrystals, accelerated both the intrinsic osteoinduction and the bone healing capacity, and significantly increased the cell-mediated resorption. These results suggest that tuning the chemical composition and the nanostructural features may allow the material to enter the physiological bone remodelling cycle, promoting a tight synchronization between scaffold degradation and bone formation.

1. Introduction

Bone is a nanocomposite material whose major constituents are collagen microfibrils and nanocrystallites of a calcium phosphate (CaP) with apatite structure. The mineral phase represents, in fact, around 65 wt% of the bone extracellular matrix.[1] This is the reason why CaPs have been the preferred option when designing synthetic bone grafts, most bone substitutes currently in the market being either hydroxyapatite (HA), beta-tricalcium phosphate (β-TCP) or a combination of both.[2]

However, although in a broad sense these materials bear some resemblance with the bone mineral, a closer look reveals major differences. Bone apatite is a highly carbonate-substituted, calcium deficient form of hydroxyapatite ($Ca_{10}(PO_4)_6(OH)_2$), with a high vacancy content,[3] and containing, in addition to carbonate, other trace elements such as Mg^{2+}, Fe^{2+}, Zn^{2+},K^{+}, Na^{+}, $(HPO_4)^{2-}$, F^{-} and Cl^{-}.[4] This results in a distorted network with poor crystallinity. The carbonate ions can substitute both hydroxyl or phosphate groups in the apatite crystal structure, originating the A-type and B-type carbonation, respectively, B-type being the preferred form in biological apatite.[3] Bone mineral is produced by precipitation from the supersaturated extracellular fluids, resulting in plate-shaped nanocrystals of variable lengths (30-50 nm) and thickness (average about 5 nm), located both within the collagen fibres, and also in the extrafibrillar space.[5] Recent studies, moreover, have shown evidence that the extrafibrillar mineral has the form of elongated plates about 5 nm thick, 60 nm wide and several hundreds of nm long.[6,7]

This is in contrast to conventional CaP bone substitutes, which are commonly obtained by high temperature sintering processes, resulting in a lack of nanostructure, and of a chemical composition far from biological apatites.[1] Although they are biocompatible and osteoconductive, their bone healing capacity is still inferior to that of autologous bone grafts, specifically in terms of the initial osteoinduction, as well as the progressive graft resorption.[8,9] In consequence, autografts are still considered the gold standard treatment, despite the major disadvantages related to the secondary harvesting surgical procedure.[10] In this work, we propose mimicking much more closely the chemical and nanostructural properties of biological apatite as a strategy to enhance the biological performance of synthetic bone grafts.

In previous studies we have shown that calcium deficient hydroxyapatite (CDHA) scaffolds can be obtained by biomimetic routes, which allow tuning not only the size but also the shape of the precipitated apatite nanocrystals.[11,12] Moreover, in order to increase the chemical similarity to natural bone, carbonate can be introduced in the apatite by a novel biomimetic process to obtain carbonated nanostructured CDHA foams.[13] This provides a very powerful platform to tailor the nanostructure and composition of biomimetic bone substitutes.

Although it was shown previously that biomimetic CDHA foams possess superior osteoinductive properties than conventional sintered ceramic foams,[14] the relevance of the nanostructure, and more specifically, the effect of nanocrystal size and morphology on the *in vivo* performance of these materials is unknown.

We recently showed through an *in vitro* study that tuning the nanostructural features of CDHA is an effective method to control the response of immune cells.[15] This is in line with other *in vitro* studies that have demonstrated that the size and shape of nanocrystals in nanostructured biomaterials exert a direct effect on cells involved in osteoinduction.[16-19] However, these results cannot be extrapolated to the very different *in vivo* scenario.

Similarly, the presence of carbonate in the apatite structure is known to increase the chemical reactivity of HA by disturbing its crystal lattice,[20-21] and it has been shown to foster osteoclastogenesis,[22-25] a critical event in the intrinsic osteoinduction cascade of biomaterials.[26,27] However, most *in vivo* studies investigating the behavior of carbonated apatites have focused on high temperature ceramics, with absence of nanostructure and limited carbonate content,[28-37] as the sintering process, in addition to fusing the nanometric crystals, causes a severe thermal decomposition of carbonate into CO_2 resulting in high carbonate losses.[38-40]

The aim of the present work was to investigate the role of nanocrystal morphology (plate *vs.* needle) and the effect of carbonate doping of nanostructured CDHA foamed scaffolds on their intrinsic osteoinduction and degradation behaviour *in vivo*, and to assess if there is a direct correlation with their bone healing capacity. To this end, the performance of nanostructured CDHA foams with two different crystal sizes and morphologies were compared using canine ectopic and orthotopic implantation models. Plate-shaped nanocrystals were compared with

needle-shaped CDHA foams evaluated in our previous studies.[14,41] To further mimic bone mineral, carbonated CDHA nanostructured foams obtained under biomimetic conditions were included as a third group.

2. Materials and Methods

2.1. Calcium phosphate materials

2.1.1. Synthesis of alpha-tricalcium phosphate powder

Alpha-tricalcium phosphate (α-TCP) powder was used as precursor of the CDHA foams, and it was synthesized as described elsewhere.[14] Then, the α-TCP particles were milled using two different milling protocols[42] in order to obtain two different sizes of α -TCP powder, a coarse powder (5.2 μm median size) and a fine powder (2.8 μm median size).

2.1.2. Preparation of foams and discs

CDHA foams were obtained by hydrolysis of α-TCP foams, as previously reported.[14,43] Fine or coarse α-TCP powders were used to obtain Fine-CDHA or Coarse-CDHA foams, respectively. The liquid to powder ratio was adjusted to obtain similar macroporosities for both type of foams, being ratios of 0.65 and 0.55 mL/g for fine and coarse α-TCP powders, respectively. Foaming was performed with a customized domestic food mixer for 30 s at 7000 rpm and the resulting foams were transferred to Teflon cylindrical moulds (5 mm diameter and 10 mm height), which were left in humid atmosphere at 37 ºC for 8 h to ensure cohesion of the foamed structures. Afterwards, the scaffolds were immersed in water for 10 days at 37 ºC to allow for the hydrolysis of α-TCP to CDHA. The carbonated CDHA foams (CO_3-CDHA) were obtained by immersing the coarse α-TCP foams in a saturated sodium bicarbonate ($NaHCO_3$, Sigma-Aldrich, St. Louis, MO) solution instead of water, in this case for 17 days to complete the hydrolysis reaction.[13]

For the *in vitro* assays, 5 mm diameter x 0.3 mm height discs were prepared of all three groups, applying the same protocol used to fabricate the foamed scaffolds, but mixing the solution in a mortar for 1 min instead of the foaming step.

2.1.3. *Materials characterization*

Phase characterization of the different samples was performed by X-ray diffraction, as previously described.[14] Samples were analyzed also by Attenuated Total Reflectance Fourier-transform infrared spectroscopy analysis (ATR-FTIR) and carbonate quantification was performed by bulk combustion element analyzer using the conditions reported in a previous study.[13] The specific surface area (SSA) was measured by nitrogen adsorption, porosity and pore entrance size distribution were quantified by mercury intrusion porosimetry (MIP), and the microstructure was determined by scanning electron microscopy (SEM) after coating the samples with carbon.[14] Finally, the macroporosity of the foamed scaffolds was characterized by micro-computed tomography (micro-CT), as described elsewhere.[14]

2.2. In vitro study

2.2.1. Cell culture

To better understand the effect of nanocrystal morphology and carbonate doping, rat mesenchymal stem cells (rMSCs) were seeded on the surface of discs of all three materials (Fine-CDHA, Coarse-CDHA and CO_3-CDHA), as previously reported.[14] Briefly, cells were expanded in AdvDMEM supplemented with 10% FBS, 20 mM HEPES buffer, 2 mM L-glutamine and penicillin/streptomycin (50 U/mL and 50µg/mL, respectively). In all experiments, cells at passages 3-4 were used.

2.2.2. Cell proliferation

For the proliferation assay, all samples were tested at 6 h, 3, 7 and 14 days. The experiments were performed with three replicates of each sample and tissue culture polystyrene (TCPS) was used as control. Cells were seeded at a density of 300 cells/mm^2. Samples were changed into another plate at each specified time and cell lysis was performed using 300 µl of M-PER® (Mammalian Protein Extraction Reagent, Thermo Scientific Inc., Waltham, MA). Subsequently, cell number was measured using the Cytotoxicity Detection KitPLUS (Hoffmann-La Roche, Basel, Switzerland) and lactate dehydrogenase (LDH) activity was determined spectrophotometrically at 492 nm (Synergy HTX, BioTek Instruments Inc., Winooski, VT). To

present the results, a calibration curve with decreasing number of cells was prepared and all values were normalized by total seeded area.

2.2.3. Cell morphology

Cell seeded discs were observed by SEM (Zeiss Neon40 EsBCrossBeam, Zeiss, Oberkochen, Germany) after 14 days. Samples were washed with PBS three times and fixed for 1 h at 4ºC in a 2.5 % glutaraldehyde (Sigma-Aldrich, St. Louis, MO) solution in PBS. Subsequently, fixed samples were washed three times with PBS and dehydrated in increasing series of ethanol solutions. Complete dehydration was performed in hexamethyldisilazane (HMDS,Thermo Scientific Inc., Waltham, MA) and discs were stored in desiccator. Dried disks were covered with a thin gold-palladium layer using vapor deposition.

Cell morphology was further analyzed by confocal microscopy using immunofluorescent staining to visualize nuclei, actin stress fibres and osteocalcin after 14 days of culture. The attached cells were rinsed with PBS (x3) and fixed in 4% paraformaldehyde (PFA, Sigma-Aldrich, St. Louis, MO) solution in PBS. Afterwards, cells were permeabilized with 0.1% Triton X-100 (Sigma-Aldrich, St. Louis, MO) in PBS for 15 min and blocked with 1% bovine serum albumin (BSA, Sigma-Aldrich, St. Louis, MO) in PBS for 1 h. Then, discs were incubated for 1 h with rabbit anti-osteocalcin (G-5, Santa Cruz Biotechnology Inc., Dallas, TX) (1:100 in 1% BSA in PBS). Subsequently, Alexa Fluor 488 chicken anti-rabbit and Alexa Fluor 546 phalloidin (Thermo Scientific Inc., Waltham, MA) were added and incubated for 1 h (1:1000 and 1:300 in 0.1% Triton X-100 in PBS, respectively). For nuclei staining, discs were incubated with 4',6-diamidino-2-phenylindole (DAPI) for 2 min. Three rinses of 5 min each in 0.15 % glycine (Sigma-Aldrich, St. Louis, MO) in PBS were done between all steps. Sample discs were mounted in Mowiol 4-88 (Sigma-Aldrich, St. Louis, MO) and visualized in a confocal microscope (Leica TCS SPE, Leica Microsystems, Wetzlar, Germany). Digital images were processed using an image analysis software (Fiji/Image-J package, open source software).

2.2.4. Cell differentiation

The osteoblastic differentiation was determined by quantifying the expression of osteogenic genes by Real-Time quantitative Polymerase Chain Reaction (RT-qPCR), as previously

reported.[14] Briefly, cells were seeded on the discs (300 cells/mm^2) and incubated for 6 h and 1 and 3 days. Additionally, for osteocalcin (OCN) late marker, 7 and 14 days were also monitored. Total RNA was extracted using RNeasy Mini Kit (Qiagen GmbH, Hilden, Germany) and quantified by NanoDrop ND-1000 spectrophotometer (NanoDrop Products, Thermo Fisher Scientific Inc., Waltham, MA). In order to ensure that cell number is not influencing the results, equal amounts of RNA (120 ng) were retrotranscribed to cDNA using the QuantiTect Reverse Transcription Kit (Qiagen GmbH, Hilden, Germany) and then specifically amplified using selective primers.[14] The expression values of studied genes were normalized by expression of β-actin, a housekeeping gene that acts as an internal control of cell number, and relative fold changes (FC) were related to tissue culture polystyrene (TCPS) at 6 h of culture, following a previously established formula.[14] The experiment was performed in two independent runs."

2.3. In vivo study

Ethical approval for the *in vivo* assays was obtained from the local ethics committee (CEAAH 2338) and all procedures were performed in compliance with the Guide for Care and Use of Laboratory Animals[44] as well as the European Community Guidelines (Directive 2010/63/EU) for the protection of animals used for scientific purposes.[45] Surgeries were performed in twelve adult beagle dogs (14-17 kg) following standard anesthetic and analgesic protocols.[14]

2.3.1. Intramuscular implantation

The intrinsic osteoinductive potential of the materials was evaluated in a standardized intramuscular canine model.[14] Briefly, once the animals were anesthetized, the lumbar skin and fascia were incised and three intramuscular pockets were created in the epaxial muscles of each dog. Subsequently, each intramuscular pocket was filled with one of the three foamed scaffolds (5 mm of diameter x 10 mm of length).

2.3.2. Intraosseous implantation

To study the bone healing capacity of the same scaffolds, their potential to repair a femoral monocortical bone defect was evaluated in a standardized intraosseous canine model,[41] in the same group of animals. Briefly, three monocortical bone defects (5 mm of diameter) were drilled

on the mid-shaft femoral diaphysis, and one scaffold (5 mm of diameter x 10 mm of length) of each group was placed in each defect by press-fit.

During the postoperative period, dogs were medicated with a long-acting antibiotic and a non steroidal anti-inflammatory drug for 7 days, which is routinely prescribed after orthopedic surgeries. Finally, six animals were euthanized at each experimental time (6 and 12 weeks post-implantation) by an overdose of pentobarbital sodium.

To sum up, one scaffold of each group (Fine-CDHA, Coarse-CDHA and CO_3-CDHA) was implanted intramuscularly and intraosseously in each dog, resulting in six intramuscular and six intraosseous scaffolds per group and evaluation time, as summarized in the Supporting Information (Figure S1).

2.3.3. Sample harvest and histological processing

After euthanasia, samples were immediately harvested and fixed in a buffered formalin solution for 72 h. The specimens were then dehydrated in a graded ethanol series, and embedded in ascending graded mixtures of ethanol and methylmethacrylate resin (Technovit 7200, Heraeus Kulzer GmbH, Hanau, Germany) that photopolymerized under white and ultraviolet light for 2 and 4 h, respectively. The resulting blocks were analyzed by micro-CT. After micro-CT scanning, each block was divided into two equal pieces. Intramuscular samples were divided transversally and intraosseous samples longitudinally to evaluate the full thickness of the cortical bone defect. One half of each sample was polished and coated with carbon for backscattered scanning electron microscopy analysis (BS-SEM).[14] The other half was sliced and grinded to obtain histological sections (50 μm). Sections were then stained with Goldner-Masson trichrome (GMT) and toluidine blue (TB) for histological evaluation.[14]

2.3.4. Histology and histomorphometry

The 3D evaluation of the samples was performed by micro-CT (SkyScan 1172, Bruker Corp., Billerica, MA), as previously established.[46] The specimen was rotated through 180º with a rotation step of 0.40º, an acquisition time of 2.1 s per scan and anisotropic pixel size of 5 μm for the intramuscular samples and 10 μm for the intraosseous samples. The same histomorphometric parameters were measured in both groups of samples:

a) Percentage of newly formed bone within the initial available macropore space:

% newly formed bone = (bone volume / initial available macropore volume) * 100

b) Percentage of scaffold degradation, calculated by subtracting the remaining scaffold volume from the initial scaffold volume prior to implantation:

% scaffold degradation = [(initial scaffold volume – final scaffold volume) / initial scaffold volume] * 100

For the intramuscular samples, both parameters were quantified in the entire scaffold volume, whereas for the intraosseous samples only the monocortical bone defect volume was considered.

The localization and maturity of the newly formed bone were determined based on tissue morphology and the different grey levels by BS-SEM imaging at a voltage of 20 kV.

The stained histological sections were observed under light microscopy (Nikon Eclipse E800, Nikon Corp.,Tokyo, Japan) to evaluate histological qualitative parameters such as the degree of peri-implant inflammatory reaction, neovascularization, fibrous-tissue infiltration and osteoclastic activity.

2.4. Statistical analysis

Data were analyzed using the GraphPad Prism Version 6.0 (GraphPad Software Inc., La Jolla, CA) and expressed as mean values ± standard error. A one-way repeated measures ANOVA followed by Tukey's post hoc test were used to detect any differences between groups and significance was considered at $p < 0.05$.

3. Results

3.1. Materials characterization

XRD analysis showed that both the foamed cylinders and the discs consisted of low crystallinity hydroxyapatite containing in some cases small amounts of unreacted α-TCP (less than 2%) (Figure 1A). The shift observed in the (300) peak (2θ shift from ~32.8° to ~33°) for the CO_3-CDHA samples indicates a contraction in the *a*-axis compared to CO_3-free samples which is consistent with a B-type carbonate substitution.[47] The ATR-FTIR spectra showed the typical phosphate bands at 570, 600, 960 and 1030 cm^{-1} for all three groups (Figure 1B).[48,49] In agreement to the XRD results, the detection of bands at 1471 and 1419 cm^{-1} in the CO_3-CDHA

samples confirmed the B-type carbonate substitution in the apatite crystal lattice in these specimens.[3,50]

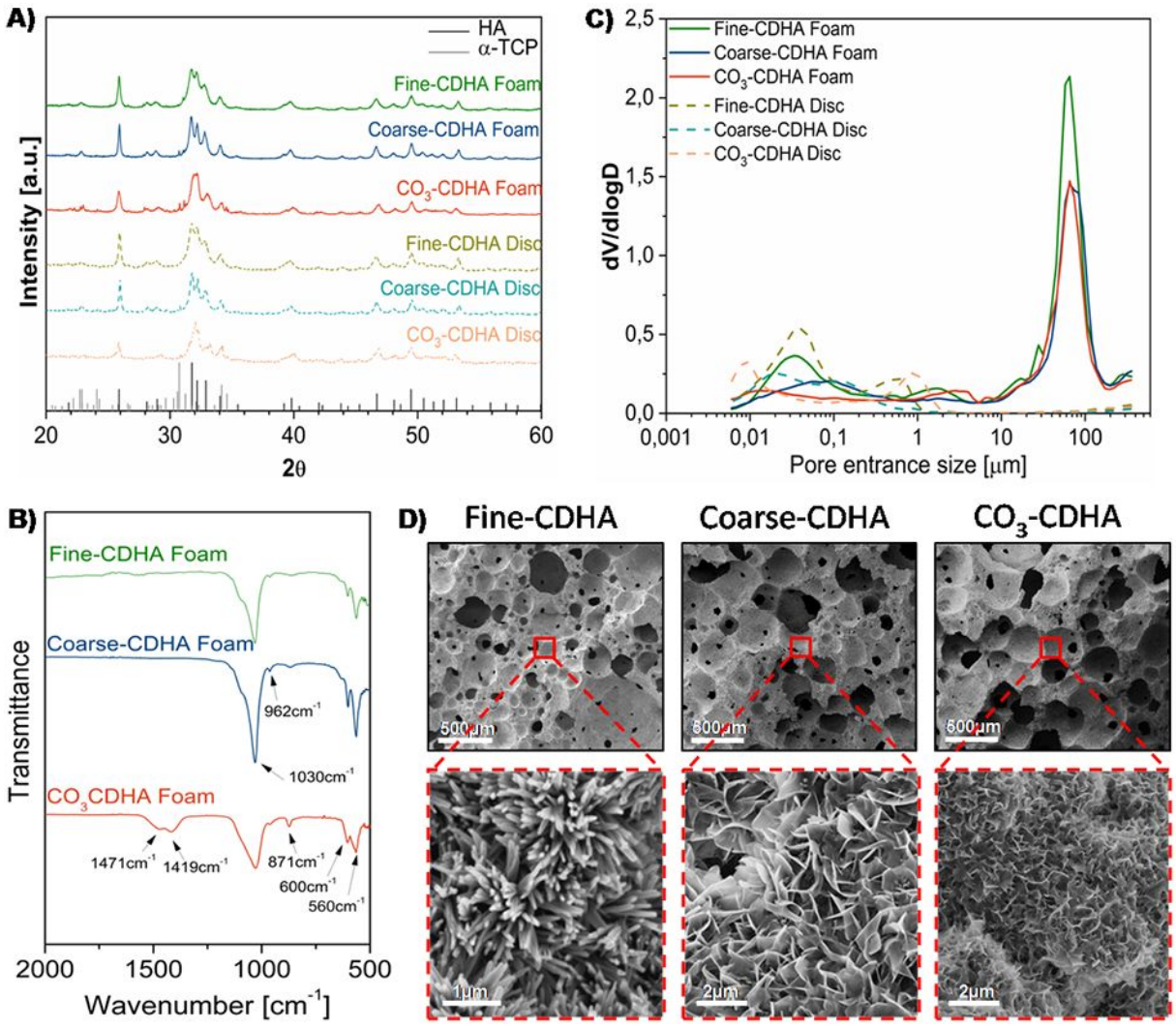

Figure 1. Physicochemical characterization of Fine-CDHA, Coarse-CDHA and CO_3-CDHA foams and discs: (A) XRD patterns. (B) ATR-FTIR spectra (C) Pore entrance size distributions determined by MIP. (D) Low magnification SEM images of the implanted foams showing the interconnected spherical concave macropores in all groups and high magnification images showing the nanostructure consisting of needle-shaped nanocrystals for the Fine-CDHA foams and plate-shaped nanocrystals for the Coarse-CDHA and CO_3-CDHA foams, smaller in the latter.

The pore entrance size distribution of the different materials, as determined by MIP, is displayed in Figure 1C. The presence of open macroporosity centered at 70 μm was confirmed in the three foamed scaffolds, together with pores in the micrometric and nanometric range. As expected, the discs, which had not been subjected to the foaming step, showed only submicrometric and nanometric pores. SEM images in Figure 1D revealed similar pore size and spherical geometry of the macropores in the three foamed materials, and marked differences in micro- and nanostructure. Whereas Fine-CDHA scaffolds showed the typical network of

entangled needle-like nanocrystals, Coarse-CDHA and CO_3-CDHA showed entangled plate-like crystals, significantly smaller in the latter.

A detailed quantification of the textural properties as well as carbonate incorporation levels is given in Table 1. SSA values varied in accordance with the nanocrystal morphology, being the highest for Fine-CDHA samples and the lowest for the Coarse-CDHA group due to the larger crystal size (Figure 1D). The carbonate content reached 11-12 wt% in the carbonated samples regardless of their dense or foamed nature, being almost negligible for the non-carbonated counterparts (Fine-CDHA and Coarse-CDHA).

Table 1. Porosity, SSA and carbonate content of the different samples

Materials		Porosity					SSA (m^2/g)	CO_3^{2-} content (wt%)
		Total Porosity by MIP (%)	Macroporosity by MIP (%)	Macroporosity by micro-CT (%)	Macropore entrance size by MIP (µm)*	Macropore size by micro-CT (µm)*		
Fine-CDHA	Disc	57.7	-	-	-	-	40.18	0.05
	Foam	76.5	49.5	52.3	70	227.0	38.49	0.03
Coarse-CDHA	Disc	51.8	-	-	-	-	21.96	0.05
	Foam	71.1	47.6	49.3	70	302.1	19.26	0.02
CO_3-CDHA	Disc	48.0	-	-	-	-	29.81	11.33
	Foam	69.7	46.7	49.1	70	264.0	30.33	12.33

*Whereas MIP determines the mean entrance size of macropores, micro-CT quantifies the mean pore size itself.

3.2. In vitro study

3.2.1. Cell adhesion and proliferation

rMSC adhesion after 6 h was very similar in all groups (Figure 2A). However, from this time point cell number progressively decreased on Fine- and Coarse-CDHA, whereas it significantly increased on CO_3-CDHA, with statistically significant differences between groups at 3, 7 and 14 days of culture.

3.2.2. Cell morphology

Morphological studies performed by SEM after 14 days of culture showed that the cells seeded on all three substrates had similar morphologies and were well spread in all cases (Figure 2B). The main difference between groups was the density of cells, in accordance with the results obtained in the proliferation assay, with lower cell density on the Coarse- and Fine-CDHA groups compared with CO_3-CDHA samples.

Immunofluorescence assays performed at 14 days revealed that actin filaments were not well developed in the cells seeded on the Coarse- and Fine-CDHA discs (Figure 2B). In contrast, cells seeded on the CO_3-CDHA discs showed clearly defined actin filaments, as well as a superior osteocalcin activity (Figure 2B), suggesting improved cell differentiation compared with the Fine- and Coarse-CDHA groups.

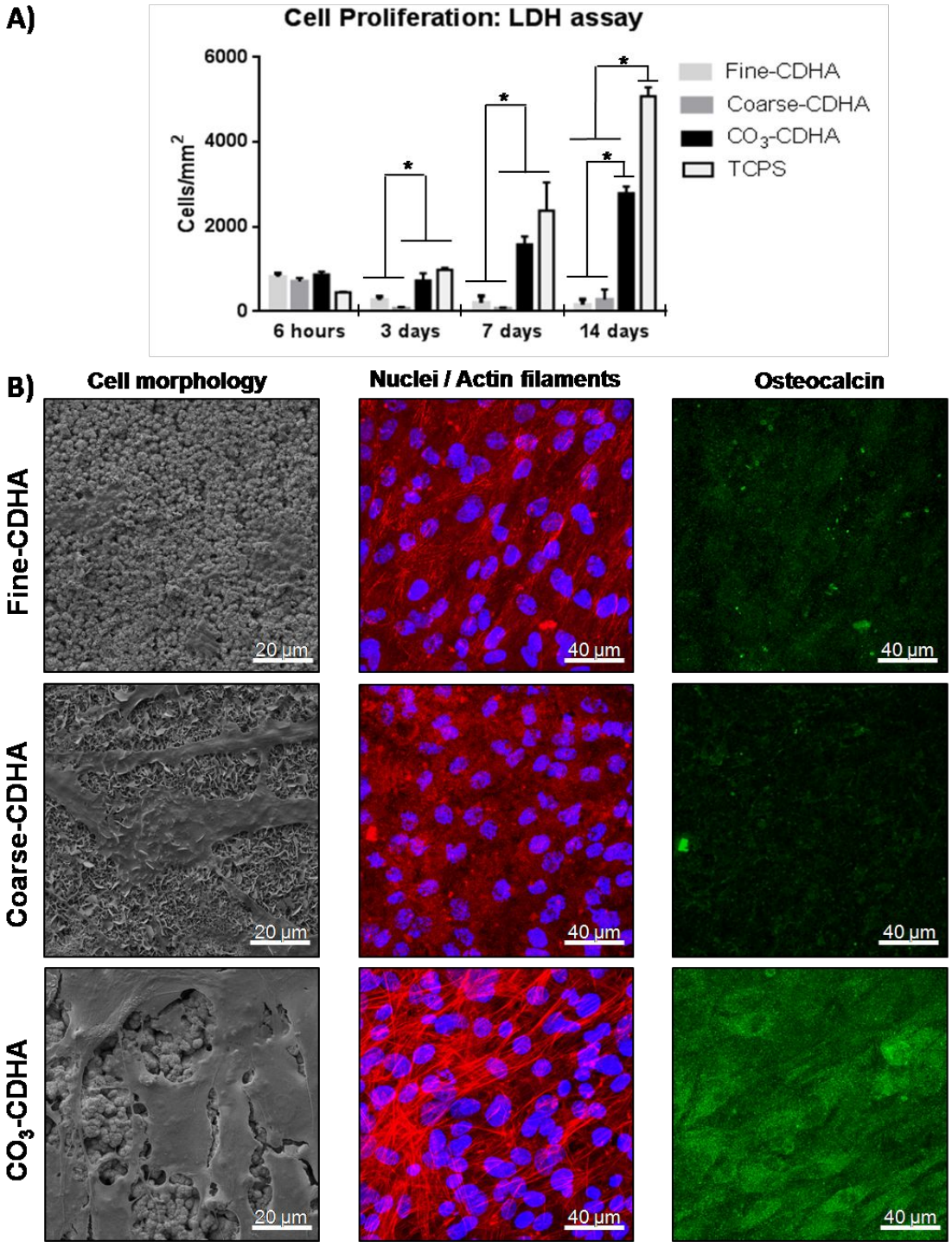

Figure 2. (A) LDH assay: rMSCs proliferation after 6 h, 3, 7 and 14 days. (*) denotes groups with statistically significant differences ($p < 0.05$). (B) Morphology of rMSCs at 14 days observed by SEM (first column) and by confocal microscopy (second and third columns). Nuclei in blue, actin fibers in red and osteocalcin in green. For osteocalcin visualization, the regions where cell were present were chosen. The confocal images are not representative in terms of cellular density for Fine-CDHA and Coarse-CDHA samples.

3.2.3. Cell differentiation

The gene expression results determined by RT-qPCR are displayed in the Supporting Information (Figure S2). In general terms, cells seeded on all three materials showed a superior osteogenic gene expression compared to those cultured on TCPS, showing significant differences at 6 h for BMP-2, Col I and OPN, at 1 day for all osteogenic markers except for ALP, and at 3 days for OPN and OCN. Moreover, the expression of OCN at 7 and 14 days was significantly higher for the cells cultured on the three CDHA discs than for those cultured on TCPS. Among the three nanostructured CDHA materials, the non-carbonated CDHA groups showed a slightly superior osteogenic gene expression than CO_3-CDHA samples, although no statistically significant differences were consistently found between groups.

3.3. In vivo study

There were no surgical and postoperative complications. No adverse foreign body reaction was observed in any case, confirming the good biocompatibility of all scaffolds in both implantation sides.

3.3.1. Intramuscular implantation

At 6 weeks, loose connective-tissue infiltration and abundant blood vessel ingrowth were observed within the interconnected macropores of all three groups (Figure 3). However, significant differences were noted regarding new ectopic bone formation. Whereas newly formed bone was found in the Fine-CDHA group in four animals out of six and in the CO_3-CDHA group in five out of six animals, no signs of bone formation were noted in the Coarse-CDHA scaffolds (Figures 3 and 4). The bone observed at 6 weeks mainly consisted in woven bone firmly attached to the concave surfaces of scaffold macropores, always formed through an intramembranous ossification process. Moreover, a few Haversian structures were observed, in which the lamellar bone was arranged concentrically around a central canal, mimicking the osteonic structure of cortical bone (Figure 3),

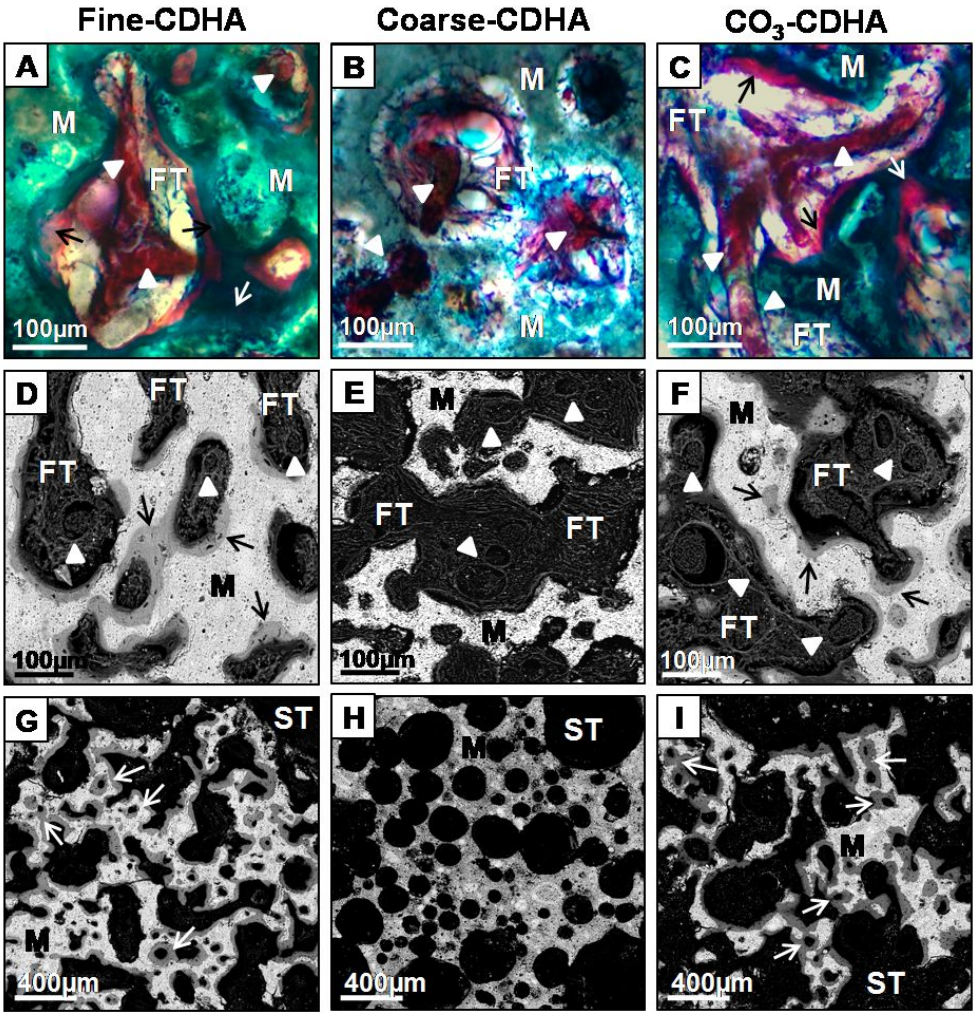

Figure 3. Undecalcified Goldner-Masson trichrome stained histological slides (A,B,C) and backscattered scanning electron micrographs (D,E,F) after 6 weeks of intramuscular implantation. All groups showed loose fibrous-tissue (FT) infiltration and abundant blood vessel (arrow heads) ingrowth within the interconnected macropores. Note the new osteoid in pink and the well-mineralized bone matrix in dark green in the GMT stained sections. In BS-SEM images the calcified bone appears in light grey. Interestingly, only Fine-CDHA and CO_3-CDHA groups showed new ectopic bone formation (arrows) at this time point, always firmly attached to the material (M) concave surfaces. (G,H,I) Backscattered scanning electron micrographs showing some Haversian structures (white arrows), in which new bone is arranged concentrically surrounding a central blood vessel replicating the osteonic structure of cortical bone. ST=Soft tissue, M=Material.

A) Bone incidence

Materials	6 weeks	12 weeks
Fine-CDHA	4/6	6/6
Coarse-CDHA	0/6	2/6
CO_3-CDHA	5/6	6/6

B) Ectopic bone formation

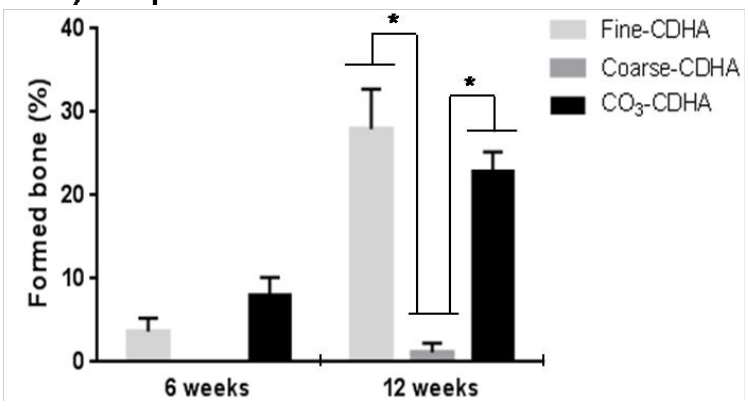

Figure 4. (A) Ectopic bone incidence after 6 and 12 weeks of intramuscular implantation. (B) Percentage of newly formed bone within the available macropore space after 6 and 12 weeks of intramuscular implantation, as determined by micro-CT. (*) Statistically significant differences between groups ($p < 0.05$).

A similar trend was observed after 12 weeks of implantation when a large amount of ectopic bone was detected in all animals for Fine-CDHA and CO_3-CDHA groups, while in the Coarse-CDHA group a reduced amount of bone was noted only in two out of six animals (Figure 4). At this time point mature lamellar bone was formed on the Fine-CDHA and CO_3-CDHA scaffolds while mainly woven bone was observed in Coarse-CDHA constructs (Figure 5).

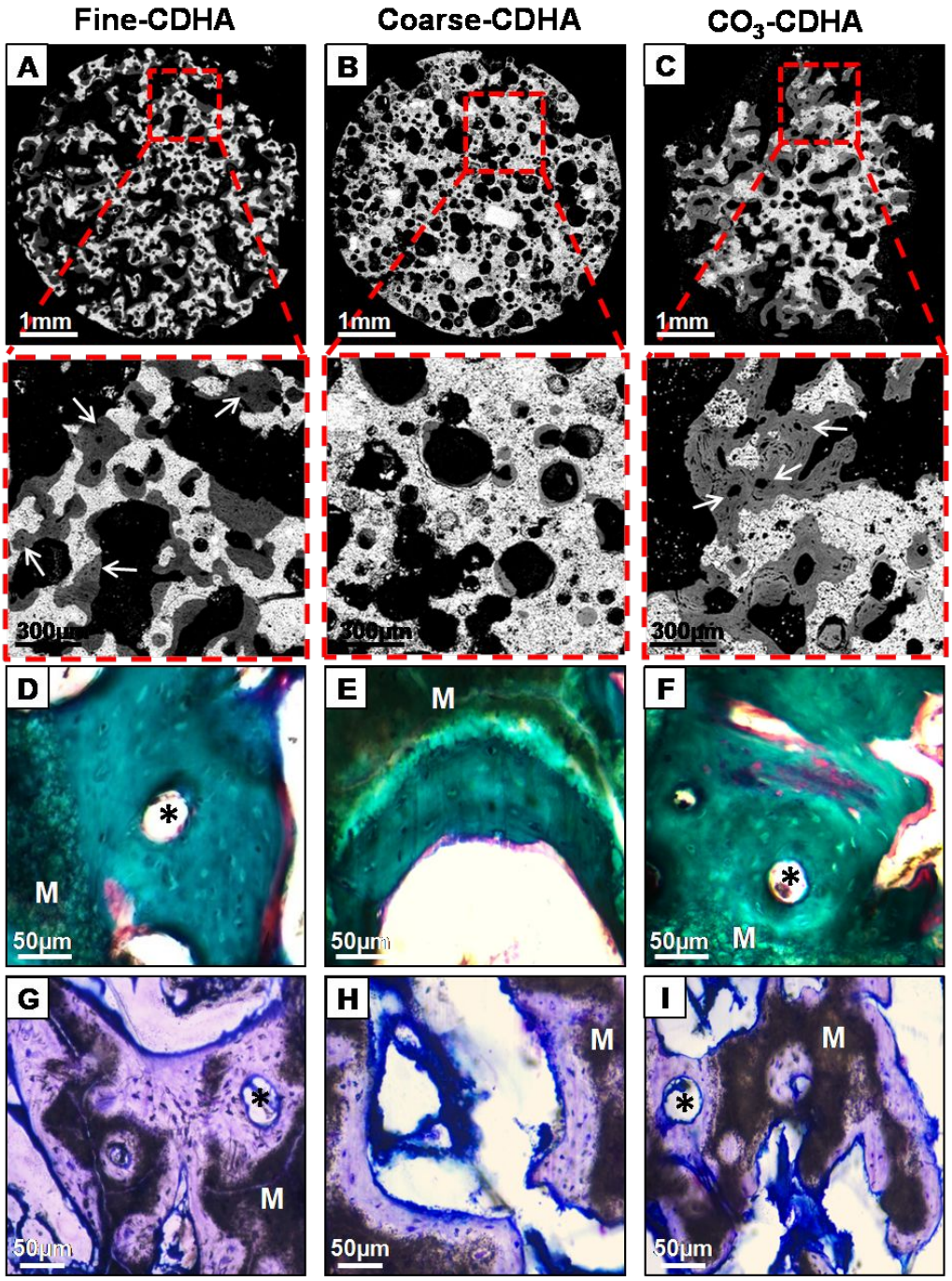

Figure 5. Histological images of the studied scaffolds after 12 weeks of intramuscular implantation. (A,B,C) Backscattered scanning electron images. (D,E,F) Undecalcified Goldner-Masson-trichrome stained histological slides. (G,H,I) Undecalcified Toluidine-blue stained histological slides. A significant amount of well-calcified bone matrix (grey in the BS-SEM, green in GMT and purple in TB) and some osteon-like structures (arrows) with the characteristic Haversian canals (asterisks) in the centre were indentified in the Fine-CDHA and CO_3-CDHA foams. In contrast, negligible amounts of ectopic bone were observed in the Coarse-CDHA constructs. Note the new osteoid (pink in GMT and blue in TB) and osteocytes inside lacunae (light green in GMT and blue in TB). M=Material.

Histological evaluation also showed the presence of multinucleated osteoclast-like resorbing cells in all samples (Figure 6C). However, a higher amount of osteoclast-like cells were observed at both time points in the Fine-CDHA scaffolds, and especially in the CO_3-CDHA scaffolds, compared with the Coarse-CDHA ones. This was in agreement with the superior degradation rate shown by the CO_3-CDHA and Fine-CDHA foams compared with the Coarse-CDHA (Figure 6A), which was more pronounced in the carbonate-containing scaffolds (Figure 6A/B), although in all cases the differences were statistically significant only after 12 weeks of implantation. It is worth noting that, contrary to the other two groups, the degradation of Coarse-CDHA constructs did not progress overtime (Figure 6A).

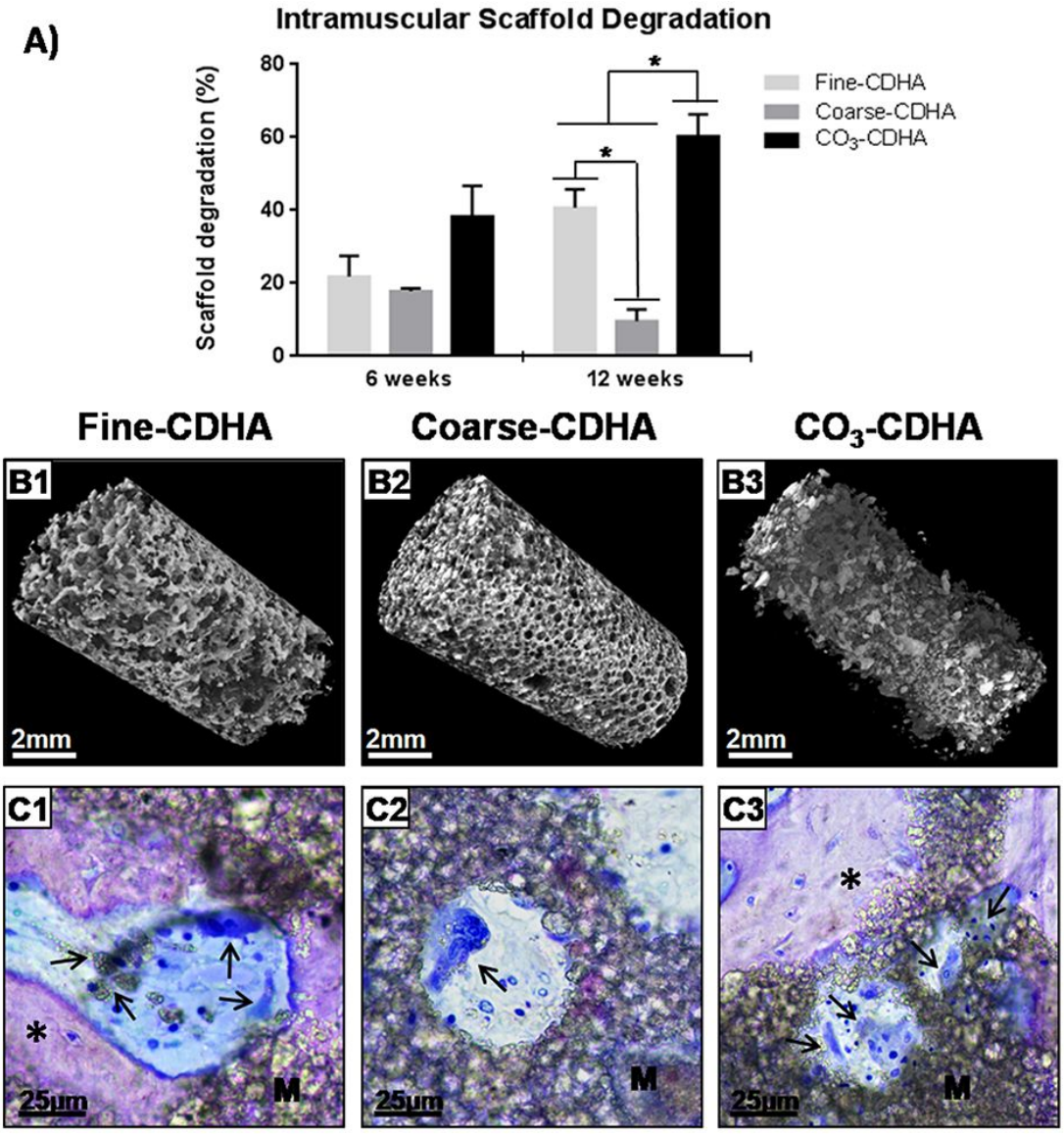

Figure 6. (A) Percentage of scaffold degradation 6 and 12 weeks after intramuscular implantation, as determined by micro-CT. (*) Statistically significant differences between groups ($p < 0.05$). (B1,B2,B3) Micro-CT 3D reconstructions of studied foams 12 weeks after intramuscular implantation. (C1,C2,C3) Undecalcified toluidine-blue stained histological slides of scaffolds implanted intramuscularly for 12 weeks showing macrophages and multinucleated osteoclast-like cells (arrows) resorbing the materials. Note intracellular material particles visible in some resorbing cells (C1,C3). M=Material, Asterisk=Ectopic bone.

3.3.2 Intraosseous implantation

Histological analysis of the scaffolds implanted orthotopically revealed new bone tissue ingrowth within open macropores of all three scaffolds, in close contact with the material surfaces and without any intervening layer of fibrous tissue at the host cortical bone-material interface (Supporting Information, Figure S3A/B/C). Moreover, all groups showed a high degree of neovascularization, as observed in the Goldner-Masson-trichrome stained sections (Supporting Information, Figure S3D/E/F).

The main histological finding, however, was that Fine-CDHA and CO_3-CDHA scaffolds stimulated bone ingrowth further, with the prompt presence of newly formed bone in the centre of the scaffolds at the early stage of 6 weeks postimplantation (Figure 7A). Conversely, in the Coarse-CDHA scaffolds new bone was formed only in the peripheral areas of the defects at this initial evaluation point (Figure 7A). After 12 weeks, complete bridging of bone defects were found for the Fine-CDHA and CO_3-CDHA scaffolds, whereas bone formation was more limited in Coarse-CDHA scaffolds and some empty pores were still noted in the central areas of the monocortical bone defects (Figure 7B).

The micro-CT histomorphometric analysis (Figure 8) confirmed the above-mentioned histological observations. Bone formation was significantly higher in the Fine-CDHA and CO_3-CDHA groups than in the Coarse-CDHA group, at both time points, as shown in Figure 8A. Moreover, Fine-CDHA and CO_3-CDHA groups exhibited also a significantly superior degradation than the Coarse-CDHA scaffolds at 12 weeks (Figure 8B). Similarly to what happened intramuscularly, the CO_3-CDHA scaffolds showed a higher resorption than Fine-CDHA constructs, especially at 12 weeks, and the resorption of Coarse-CDHA scaffolds did not progress significantly overtime (Figure 8B).

The consistent observation of cutting cones and osteoclast-like cells in all groups was a clear indication of cell-mediated scaffold resorption and the integration of the material in the bone remodelling process (Supporting Information, Figure S3G/H/I). However, similarly to the intramuscular study, osteoclast-like cells were more abundant in the Fine-CDHA, and especially in the CO_3-CDHA scaffolds, than in the Coarse-CDHA foams at both time points.

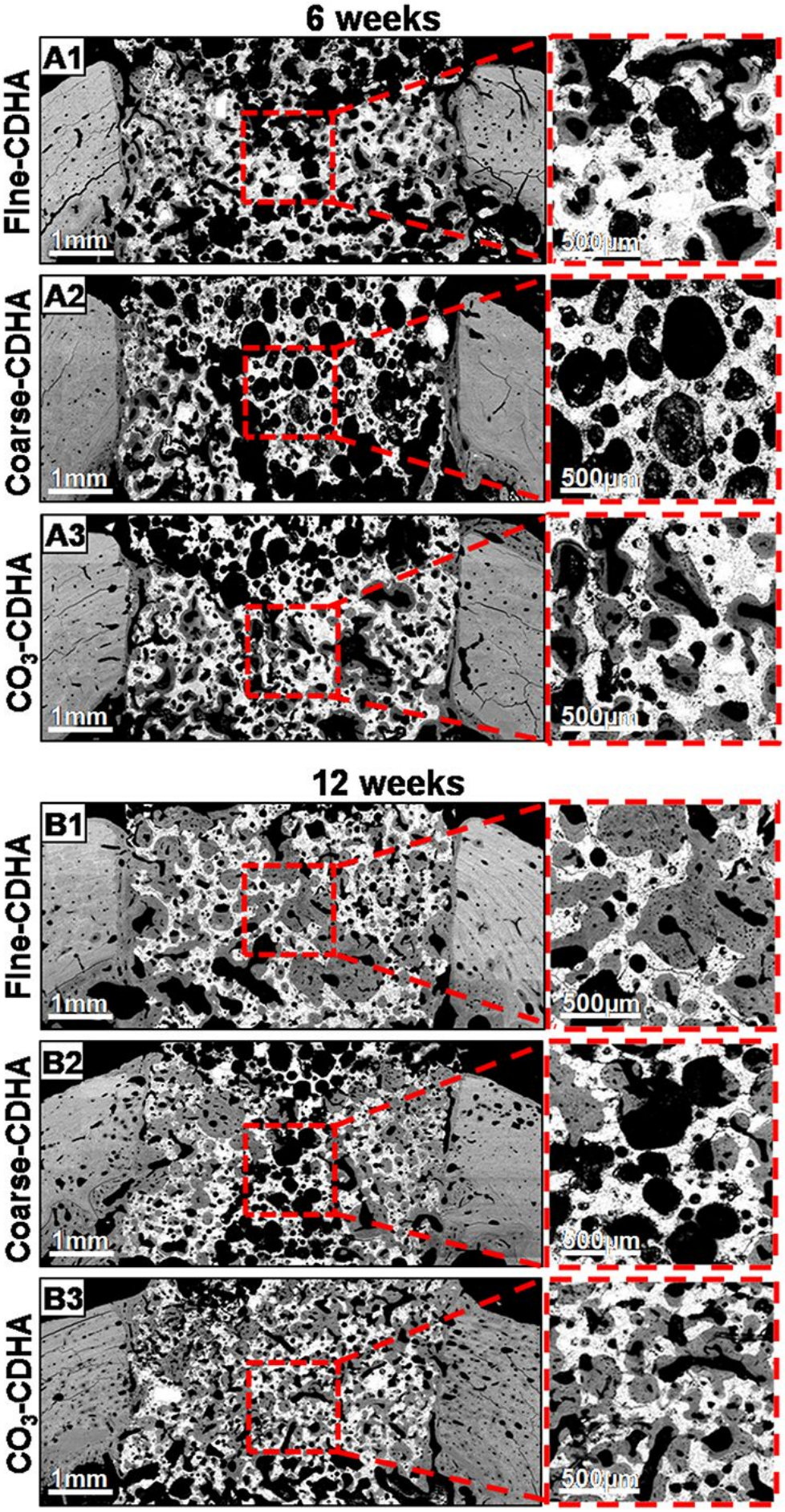

Figure 7. Backscattered scanning electron micrographs of a section of the femoral diaphysis, showing the cortical bone containing the studied scaffolds, after 6 (A1,A2,A3) and 12 weeks (B1,B2,B3) of implantation.

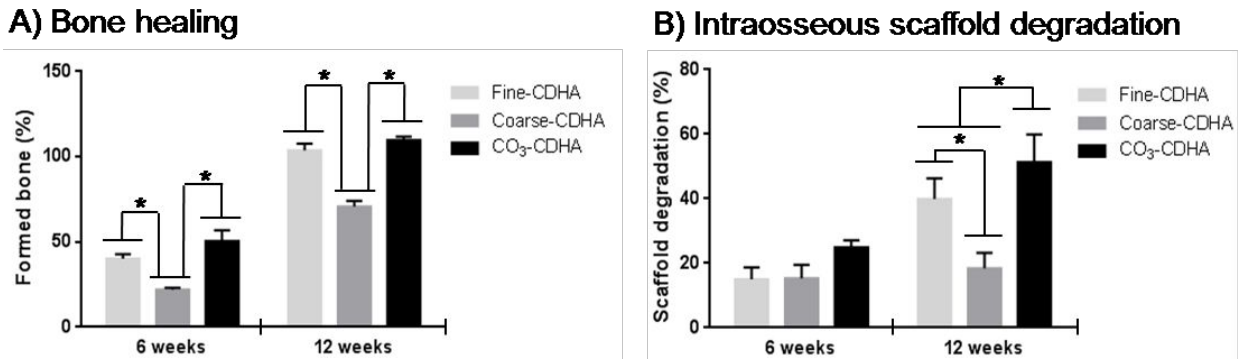

Figure 8. Histomorphometrical results obtained by micro-CT after 6 and 12 weeks of intraosseous implantation: (A) Percentage of new bone within the monocortical bone defect. (B) Percentage of scaffold degradation. (*) Statistically significant differences between groups ($p < 0.05$).

4. Discussion

The fabrication of CaP scaffolds using biomimetic routes, based on the hydrolysis of α-TCP to a CDHA at body temperature, and avoiding high temperature sintering processes, allowed mimicking the properties of bone mineral. As shown in Figure 1, it was possible to tune the microstructure and the chemical composition of the biomimetic CDHA, modifying crystal shape and size, and consequently the textural properties of the materials. Using α-TCP powders of different sizes, either fine or coarse, allowed obtaining CDHA nanocrystals with different morphologies, either thin needles about 30-60 nm thick and 300-500 nm long or thin submicrometric plates about about 100 nm thick and 700-900 nm wide, respectively, with a consequent change in the SSA from 40 m^2/g to 20 m^2/g (Figure 1D and Table 1). Although the crystals obtained were still slightly larger than the ones found in the bone mineral, the biomimetic route allowed approaching closely the size and morphology of biological apatite.

Concerning chemical composition, in order to increase the biomimetism of the foams, carbonation of the scaffolds was achieved by performing the setting reaction of the coarse α-TCP foams in a carbonate-containing solution. This resulted in the incorporation of carbonate in the CDHA structure as revealed by the displacement of the XRD peaks and the appearance of the bands in the ATR-FTIR spectra corresponding to B-type carbonated CDHA, the preferred type of carbonate substitution in bone apatite.[3,4,36] The amount of carbonate introduced in the CDHA was 11-12%, slightly higher than the amount contained in bone apatite, which ranges between 4 and 8% depending on the age.[51] This was accompanied with a change in

microstructure, since small plate-like nanocrystals with intermediate SSA (around 30 m^2/g) were obtained (Figure 1D and Table 1), in agreement with previous studies.[13]

The effects of both nanostructure and carbonate substitution in terms of osteoinduction and bone healing potential are discussed in the following sections.

4.1 Effect of nanostructure and carbonate doping on osteoinduction

The foams analyzed in the present study presented similar macropore architecture, that is, similar percentage of total porosity, macropore volume, macropore geometry, macropore entrance size and macropore size values (Figure 1D and Table 1). The good macropore interconnectivity fostered a fast neovascularization in all scaffolds (Figure 3). In contrast, very different trends were observed in terms of osteoinduction depending on nanostructure and chemical composition. After the intramuscular implantation of the scaffolds for 6 weeks, Coarse-CDHA constructs did not show any sign of ectopic bone formation, while both Fine-CDHA and CO_3-CDHA exhibited high incidences of ectopic bone formation, being slightly higher for the carbonated foams (Figures 3 and 4). Moreover, at 12 weeks postimplantation, these two groups showed a considerable amount of newly formed ectopic bone in all dogs, whereas only a small amount of ectopic bone was observed in 2 out of 6 animals in the Coarse-CDHA group (Figures 4 and 5). Considering that the three groups shared the same macropore features, the significant differences observed in their osteoinductive potential should be ascribed to the nanostructure and composition of the materials. The smaller nanocrystals of the Fine-CDHA and CO_3-CDHA scaffolds, with the associated larger SSAs compared to the Coarse-CDHA scaffolds, are known to enhance surface reactivity increasing the capacity to release calcium and phosphate ions upon cell-mediated degradation. Moreover, the reactivity is further promoted by the presence of carbonate ions (Figures 6A and 8B). These findings go in the same direction as previous *in vivo* studies,[52-54] which showed that increasing the microporosity fostered osteoinduction of CaPs, although the range of SSAs analyzed were significantly smaller than the ones studied in the present work.

The in vitro study with rMSCs showed some contradictory results. A higher cell proliferation (Figure 2A) and more mature cell morphology (Figure 2B) was observed for the cells seeded on CO_3-CDHA discs compared with both Fine-and Coarse-CDHA discs. The low proliferation on

Fine- and Coarse-CDHA agrees with previous results and was associated to the specific chemical and topographical features of these materials.[55] It is important to mention that phalloidin stains F-actin, present in well-organized cytoskeleton, as observed in CO_3-CDHA samples. The blurry staining observed in Fine- and Coarse-CDHA indicates a poorly organized cytoskeleton usually associated to immature focal adhesions and reduced cell proliferation.[56] However, the RT-qPCR analysis showed, as a general trend, higher expression of osteogenic genes for the cells cultured on Fine- and Coarse-CDHA than on CO_3-CDHA samples, with no significant differences between the two undoped CDHA substrates (Supporting Information, Figure S2). This enhanced differentiation may also contribute to the reduction in cell proliferation.[57] In general, gene expression increased between 6 h and 1 d of incubation, decreasing afterwards, as observed in previous studies.[56] The increase in OCN gene expression at day 3 motivated the analysis of this gene at longer periods of incubation. Interestingly, these results were obtained without the addition of osteogenic medium, indicating that differentiation was induced by the topographical and chemical features of the CDHA surface, since no significant ionic fluctuations in the cell culture medium were observed (Supporting Information, Figure S4)."

These results, which can seem contradictory when compared with the ectopic bone formation, are a clear indication of the limitations of the static *in vitro* cell cultures to model the *in vivo* scenario, and reveal that the mechanism leading to osteoinduction cannot be reduced to a simple and direct interaction between material and MSCs. The mechanism is in fact far more complex and involves numerous intermediate processes and interactions, which are overlooked in a simple *in vitro* MSC cell culture study. Indeed, some studies have already proved the key role played by macrophages and osteoclasts in osteoinduction.[26,27,53] The osteogenic growth factors secreted by these cells,[58-61] together with the release of calcium and phosphate ions when resorbing the materials,[62-65] are deemed to trigger the osteogenic differentiation of MSCs. In this line, we analyzed in a recent *in vitro* study the effect of different nanostructures of biomimetic CDHA on osteoimmunomodulation. We observed that macrophages were sensitive to the nanostructural features and, when cultured on needle-like Fine-CDHA substrates, the cytokines generated by macrophages were able to trigger osteoblastic differentiation and osteogenesis.[15]

Regarding the degradation behavior, large differences were observed between the different foams, despite the identical or similar chemical composition between groups. Coarse-CDHA foams, with the lowest SSA, were the least resorbable scaffolds, being the only group where scaffold resorption did not progress overtime (Figure 6A). In contrast, Fine-CDHA and CO_3-CDHA scaffolds showed a superior and progressive resorption, with statistically significant differences at 12 weeks compared with Coarse-CDHA constructs (Figure 6A). Since body fluids are supersaturated regarding CDHA and CO_3-CDHA, the degradation observed should be attributed to cell activity. In fact, a larger number of osteoclast-like cells were detected in both groups compared with that observed in Coarse-CDHA samples.

Two different parameters can contribute to a higher cell-mediated degradation of a scaffold: i) the presence of a larger number of bone-resorbing cells, in this case osteoclast-like multinucleated cells; ii) the higher sensitivity of the material to the acidic pH produced by the bone-resorbing cells. Regarding the first factor, a higher number of osteoclast-like cells were observed both in the Fine- and CO_3-CDHA foams compared with the Coarse-CDHA scaffolds in the histological analysis, which would contribute to the higher degradation rate observed in those groups. On top of this, the susceptibility of the biomaterial to acidic degradation is typically affected by the SSA and the chemical composition of the substrate. Thus, foams with higher SSA (i.e., Fine- and CO_3-CDHA foams) are more reactive, and therefore more susceptible to acidic degradation. With regards to changes in the chemical composition, despite carbonate incorporation in the crystal lattice of stoichiometric HA is well known to disturb the crystal lattice enhancing reactivity,[20,21,36] we were able to prove in an earlier work that carbonate incorporation in an already distorted calcium deficient HA did not have much influence on reactivity.[13] Thus, we believe that the superior degradation of the carbonate containing foams implies a major recruitment of osteoclast-like cells on this particular substrate.

Previous *in vitro*[22,23,25] and *in vivo* studies[24,29,30,32,35] already reported the promotion of the osteoclastic activity by natural or synthetic carbonated apatites. The results found in the present work demonstrate that both carbonate content and SSA can be used to tune degradation. However, the fact that carbonate doping entailed also a change in crystal size and SSA

precluded the possibility to evaluate independently the effect of carbonate doping and textural properties.

Interestingly, the higher activity of osteoclastic-like cells observed in the Fine- and CO_3-CDHA foams was associated to a superior osteoinductive potential compared to the Coarse-CDHA constructs. This, indeed, contrasts to previous works, in which the high resorption rate showed by carbonated apatite scaffolds, instead of being beneficial for osteoinduction, definitely hindered it.[33,34,36] Carbonated apatites with a SSA of 7-10 m^2/g and 3-8 wt% of carbonate were claimed to lack the stable three-dimensional network needed to enable bone formation,[33,34,36] and it was postulated that there was a maximum SSA that beneficially affects osteoinduction.[33] In contrast, the nanostructured Fine- and CO_3-CDHA analyzed in this work, with much higher SSA values (30-40 m^2/g), as well as a higher carbonate content (12 wt%) in the case of CO_3-CDHA, simultaneously presented high rates of resorption and large amounts of bone formation in an ectopic site.

4.2 Effect of nanostructure and carbonate doping on bone healing

In order to assess the correlation between the osteoinductive potential and bone healing capacity, the same biomaterials were implanted orthotopically in the same dogs used for the intramuscular implantation study. Histological evaluation indicated that all scaffolds were well integrated in the cortical bone without any inflammatory adverse reaction. Similarly to what was observed intramuscularly, all groups showed a widespread angiogenesis within the macropores of the constructs (Supporting Information, Figure S3), which confirmed the appropriate pore interconnectivity, as well as the good biocompatibility of all three types of scaffolds, as previously reported in similar *in vivo* studies were CDHA[66-68] and carbonated hydroxyapatite[24,29,32,35,36] were evaluated orthotopically.

The main finding was that the scaffolds with higher osteoinductivity, namely Fine-CDHA and CO_3-CDHA, accelerated and promoted osteogenesis orthotopically (Figure 7), as demonstrated by the significantly higher percentage of newly formed bone after 6 and 12 weeks compared with the poorly osteoinductive Coarse-CDHA constructs (Figure 8A). Interestingly, whereas considerable bone ingrowth was indentified in the peripheral regions of all scaffolds, as a result of their excellent osteoconductive properties triggered by the open and interconnected

macropores, negligible amounts of bone were noted in the centre of the Coarse-CDHA scaffolds at 6 weeks (Figure 7A). In contrast, the early presence of new bone formation in the centre of the bone defects treated with the Fine- and CO_3-CDHA scaffolds (Figure 7A) could be ascribed to the high intrinsic osteoinductive capacity of these materials, demonstrated in the ectopic implantation experiment. At 12 weeks, the results followed the same trend, as Fine- and CO_3-CDHA scaffolds exhibited a complete bone bridging and filling the full-thickness of cortical defects, whereas bone formation was significantly inferior in the Coarse-CDHA scaffolds (Figure 7B and 8A). It is worth mentioning that a good correlation among osteoinduction and bone healing capacity has been described in previous studies for sintered ceramics.[36,69,70]

A good match was found also when comparing the resorption behaviour in orthotopic and ectopic sites (Figures 6A and 8B). Fine-CDHA scaffolds promoted a significantly higher cell-mediated resorption than Coarse-CDHA scaffolds after 12 weeks of implantation, being even higher in the CO_3-CDHA group (Figure 8B). The resorption of Coarse-CDHA constructs implanted intraosseously did not progress overtime (Figure 8B), as already observed intramuscularly. The high cell-mediated resorption exhibited by the Fine-CDHA and, especially, by the CO_3-CDHA scaffolds, in conjunction with their high osteoconductive and osteoinductive properties enabled an excellent synchronization between biomaterial resorption and new bone formation. This resulted in a percentage of newly formed bone at 12 weeks over a hundred per cent in these two groups (Figure 8A), since the percentage was calculated over the initial macropore volume. The macropore volume after implantation was greater than the initial one, and it was almost fully occupied by new bone.

Overall, the present results highlight on one side the importance of the nanocrystal morphology and SSA and suggest that there is a threshold value in terms of SSA necessary to activate the cell-mediated resorption and the associated osteoinductive potential, which determine the osteogenic capacity of the materials in a bony environment. Regarding the effect of carbonate doping, although it is not possible to separate it from the textural properties since its inclusion in the apatite entails also a change in crystal morphology and an increase in SSA, it clearly increases degradation without impairing the osteoinductive properties.

5. Conclusions

The results obtained in the present study demonstrate that the idea of mimicking the mineral phase of bone is a powerful approach to design bone substitutes with enhanced performance. The size and morphology of the nanocrystals, as well as the presence of carbonate, allow tuning the osteoinductive and osteogenic potentials as well as the degradation profile of the CDHA. Moreover, those materials with textural and compositional properties closer to the biological apatite exhibited better synchronization between material resorption and bone formation. This suggests that biomimetic CDHA is able to enter the natural bone remodeling process, being transformed by the cells using the same mechanisms by which they remodel the extracellular matrix. Further studies are required in order to verify this hypothesis and clarify the underlying mechanisms, and the interactions of the material with the host tissue at a cellular and molecular level.

Associated Content

Supporting Information

Supporting Information is available free of charge on the ACS Publications website at DOI: XXX

Summary of implanted samples; gene expression results of cell differentiation *in vitro* assay; histological images of intraosseously implanted scaffolds; calcium and phosphate concentrations of cell culture medium (PDF)

Author Information

Corresponding Author

*E-mail: maria.pau.ginebra@upc.edu

Notes

The authors declare no competing financial interest.

Acknowledgments

Authors acknowledge financial support to the Spanish Government through the MAT2015-65601-R Project, co-funded by the EU through European Regional Development Funds, the Catalan Government through 2017SGR1165 Project and the Swedish Foundation for

International Cooperation in Research and Higher Education (STINT, GA IG2011-2047). AB acknowledges a FPU scholarship from the Spanish Ministry of Education and ME acknowledges support from the Serra Hunter programme. Support for the research of MPG was received through the ICREA Academia award for excellence in research funded by the Generalitat de Catalunya. Authors would like to express their gratitude to Dr. Trifon Trifonov from Barcelona Research Center in Multiscale Science and Engineering at Universitat Politècnica de Catalunya for his technical assistance with BS-SEM analysis and Susanne Lewin from Materials in Medicine Group at Uppsala University for her technical assistance with micro-CT analysis.

References

(1) Wopenka, B.; Pasteris, J. D. A Mineralogical Perspective on the Apatite in Bone. *Mater. Sci. Eng. C* **2005**, 25, 131-143.

(2) Chai, Y. C.; Carlier, A.; Bolander, J.; Roberts, S. J.; Geris, L.; Schrooten, J.; Van Oosterwyck, H.; Luyten, F. P. Current Views on Calcium Phosphate Osteogenicity and the Translation into Effective Bone Regeneration Strategies. *Acta Biomater.* **2012**, 8, 3876-3887.

(3) Rey, C.; Collins, B.; Goehl, T.; Dickson, I. R.; Glimcher, M. The Carbonate Environment in Bone Mineral: A Resolution-Enhanced Fourier Transform Infrared Spectroscopy Study. *Calcif. Tissue Int.* **1989**, 45, 157-164.

(4) Bigi, A.; Cojazzi, G.; Panzavolta, S.; Ripamonti, A.; Roveri, N.; Romanello, M.; Noris-Suarez, K.; Moro, L. Chemical and Structural Characterization of the Mineral Phase from Cortical and Trabecular Bone. *J. Inorg. Biochem.* **1997**, 68, 45-51.

(5) Reznikov, N.; Shahar, R.; Weiner, S. Bone Hierarchical Structure in Three Dimensions. *Acta Biomater.* **2014**, 10, 3815-3826.

(6) McNally, E.; Schwarcz, H. P.; Botton, G. A.; Arsenault, A. L. A Model for the Ultra-Structure of Bone Based on Electron Microscopy of Ion-Milled Sections. *PLos One* **2012**, 7, e29258.

(7) Schwarcz H. P. The Ultrastructure of Bone as Revealed in Electron Microscopy of Ion-Milled Sections. *Semin. Cell Dev. Biol.* **2015**, 46, 44-50.

(8) Habibovic, P. Strategic Directions in Osteoinduction and Biomimetics. *Tissue Eng. Part A* **2017**, 23, 1295-1296.

(9) Barradas, A. M. C.; Yuan, H.; van Blitterswijk, C. A.; Habibovic, P. Osteoinductive Biomaterials: Current Knowledge of Properties, Experimental Models and Biological Mechanisms. *Eur. Cell. Mater.* **2011**, 21, 407-429.

(10) Younger E. M.; Chapman, M. W. Morbidity at Bone Graft Donor Sites. *J. Orthop. Trauma.* **1989**, 3, 92-95.

(11) Ginebra, M. P.; Driessens, F. C. M.; Planell, J. A. Effect of the Particle Size on the Micro and Nanostructural Features of a Calcium Phosphate Cement: a Kinetic Analysis. *Biomaterials* **2004**, 25, 3453-3462.

(12) Pastorino, D.; Canal, C.; Ginebra, M. P. Multiple Characterization Study on Porosity and Pore Structure of Calcium Phosphate Cements. *Acta Biomater.* **2015**, 28, 205-214.

(13) Diez-Escudero, A.; Espanol, M.; Beats, S.; Ginebra, M. P. In Vitro Degradation of Calcium Phosphates: Effect of Multiscale Porosity, Textural Properties and Composition. *Acta Biomater.* **2017**, 60, 81-92.

(14) Barba, A.; Diez-Escudero, A.; Maazouz, Y.; Rappe, K.; Espanol, M.; Montufar, E. B.; Bonany, M.; Sadowska, J. M.; Guillem-Marti, J.; Öhman-Mägi, C.; Persson, C.; Manzanares, M. C.; Franch, J.; Ginebra, M. P. Osteoinduction by Foamed and 3D-Printed Calcium Phosphate Scaffolds: Effect of Nanostructure and Pore Architecture. *ACS Appl. Mater. Interfaces* **2017**, 9, 41722-41736.

(15) Sadowska, J. M.; Wei, F.; Guo, J.; Guillem-Marti, J.; Ginebra, M. P.; Xiao, Y. Effect of Nano-Structural Properties of Biomimetic Hydroxyapatite on Osteoimmunomodulation. *Biomaterials* **2018**, 181, 318-332.

(16) Dalby, M. J.; Gadegaard, N.; Tare, R.; Andar, A.; Riehle, M. O.; Herzyk, P.; Wilkinson, C. D.; Oreffo, R. O. The Control of Human Mesenchymal Cell Differentiation Using Nanoscale Symmetry and Disorder. *Nat. Mater.* **2007**, 6, 997-1003.

(17) Engel, E.; Del Valle, S.; Aparicio, C.; Altankov, G.; Asin, L.; Planell, J. A.; Ginebra, M. P. Discerning the role of topography and ion exchange in cell response of bioactive tissue engineering scaffolds. *Tissue Eng. Part A*. **2008**, 14, 1341-1351.

(18) Danoux, C.; Pereira, D.; Döbelin, N.; Stähli, C.; Barralet, J.; van Blitterswijk, C.; Habibovic, P. The Effects of Crystal Phase and Particle Morphology of Calcium Phosphates on Proliferation and Differentiation of Human Mesenchymal Stromal Cells. *Adv. Healthc. Mater.* **2016**, 5, 1775-1785.

(19) Dobbenga, S.; Fratila-Apachitei, L. E.; Zadpoor, A. A. Nanopattern-Induced Osteogenic Differentiation of Stem Cells - A Systematic Review. *Acta Biomater.* **2016**, 46, 3-14.

(20) LeGeros, R. Z. Effect of Carbonate on the Lattice Parameters of Apatite. *Nature* **1965**, 206, 403-404.

(21) Okazaki, M.; Moriwaki, Y.; Aoba, T.; Doi, Y.; Takahashi, J. Solubility Behavior of CO_3 Apatites in Relation to Crystallinity. *Caries Res*. **1981**, 15, 477-483.

(22) Doi, Y.; Shibutani, T.; Moriwaki, Y.; Kajimoto, T.; Iwayama, Y. Sintered Carbonate Apatites as Bioresorbable Bone Substitutes. *J. Biomed. Mater. Res*. **1998**, 39, 603-610.

(23) Spence, G.; Patel, N.; Brooks, R.; Bonfield, W.; Rushton, N. Osteoclastogenesis on Hydroxyapatite Ceramics: the Effect of Carbonate Substitution. *J. Biomed. Mater. Res. A* **2010**, 92, 1292-1300.

(24) Ayukawa, Y.; Suzuki, Y.; Tsuru, K.; Koyano, K.; Ishikawa, K. Histological Comparison in Rats between Carbonate Apatite Fabricated from Gypsum and Sintered Hydroxyapatite on Bone Remodeling. *Biomed. Res. Int.* **2015**, 2015, 579541.

(25) Pernelle, K.; Imbert, L.; Bosser, C.; Auregan, J. C.; Cruel, M.; Ogier, A.; Jurdic, P.; Hoc, T. Microscale Mechanical and Mineral Heterogeneity of Human Cortical Bone Governs Osteoclast Activity. *Bone* **2017**, 94, 42-49.

(26) Klar, R. M.; Duarte, R.; Dix-Peek, T.; Dickens, C.; Ferretti, C.; Ripamonti, U. Calcium Ions and Osteoclastogenesis Initiate the Induction of Bone Formation by Coral-Derived Macroporous Constructs. *J. Cell. Mol. Med.* **2013**, 17, 1444-1457.

(27) Davison, N. L.; Gamblin, A. L.; Layrolle, P.; Yuan, H.; de Bruijn, J. D.; Barrère-de Groot, F. Liposomal Clodronate Inhibition of Osteoclastogenesis and Osteoinduction by Submicrostructured Beta-Tricalcium Phosphate. *Biomaterials* **2014**, 35, 5088-5097.

(28) Manjubala, I.; Sivakumar, M.; Sureshkumar, R. V.; Sastry, T. P. Bioactivity and osseointegration study of calcium phosphate ceramic of different chemical composition. *J. Biomed. Mater. Res*. **2002**, 63, 200-208.

(29) Hasegawa, M.; Doi, Y.; Uchida, A. Cell-mediated bioresorption of sintered carbonate apatite in rabbits. *J. Bone Joint Surg. Br.* **2003**, 85, 142-147.

(30) Landi, E.; Celotti, G.; Logroscino, G.; Tampieri, A. Carbonated Hydroxyapatite as Bone Substitute. *J. Eur. Ceram. Soc.* **2003**, 23, 2931-2937.

(31) Porter, A.; Patel, N.; Brooks, R.; Best, S.; Rushton, N.; Bonfield, W. Effect of Carbonate Substitution on the Ultrastructural Characteristics of Hydroxyapatite Implants. *J. Mater. Sci. Mat. Med.* **2005**, 16, 899-907.

(32) Kogaya, Y.; Hasegawa, M.; Uchida, A.; Doi Y. Ultrastructural Characterization of Tissue Response to Sintered Carbonate Apatite in Rabbit Bone. *Dent. Mater. J.* **2006**, 25, 487-492.

(33) Habibovic, P.; Sees, T. M.; van den Doel, M. A.; van Blitterswijk, C. A.; de Groot, K. Osteoinduction by Biomaterials-Physicochemical and Structural Influences. *J. Biomed. Mater. Res. A* **2006**, 77, 747-762.

(34) Habibovic, P.; Kruyt, M. C.; Juhl, M. V.; Clyens, S.; Martinetti, R.; Dolcini, L.; Theilgaard, N.; van Blitterswijk, C. A. Comparative in Vivo Study of Six Hydroxyapatite-Based Bone Graft Substitutes. *J. Orthop. Res.* **2008**, 26, 1363-1370.

(35) Keiichi, K.; Mitsunobu, K.; Masafumi, S.; Yutaka, D.; Toshiaki, S. Induction of New Bone by Basic FGF-Loaded Porous Carbonate Apatite Implants in Femur Defects in Rats. *Clin. Oral Implants Res*. **2009**, 20, 560-565.

(36) Habibovic, P.; Juhl, M. V.; Clyens, S.; Martinetti, R.; Dolcini, L.; Theilgaard, N.; van Blitterswijk, C. A. Comparison of Two Carbonated Apatite Ceramics in Vivo. *Acta Biomater.* **2010**, 6, 2219-2226.

(37) Kasai, T.; Sato, K.; Kanematsu, Y.; Shikimori, M.; Kanematsu, N.; Doi, Y. Bone Tissue Engineering Using Porous Carbonate Apatite and Bone Marrow Cells. *J. Craniofac. Surg.* **2010**, 21, 473-478.

(38) Barralet, J. E.; Knowles, J. C.; Best, S. M.; Bonfield, W. Thermal Decomposition of Synthesised Carbonate Hydroxyapatite. *J. Mater. Sci. Mater. Med.* **2002**, 13, 529-533.

(39) Rau, J. V.; Cesaro, S. N.; Ferro, D.; Barinov, S. M.; Fadeeva, I. V. FTIR Study of Carbonate Loss from Carbonated Apatites in the Wide Temperature Range. J*. Biomed. Mater. Res. B Appl. Biomater.* **2004**, 71, 441-447.

(40) Barinov, S. M.; Rau, J. V.; Cesaro, S. N.; Durisin, J.; Fadeeva, I. V.; Ferro, D.; Medvecky, L.; Trionfetti, G. Carbonate Release from Carbonated Hydroxyapatite in the Wide Temperature Range. *J. Mater. Sci. Mater. Med.* **2006**, 17, 597-604.

(41) Barba, A.; Maazouz, Y.; Diez-Escudero, A.; Rappe, K.; Espanol, M.; Montufar, E. B.; Persson, C.; Öhman-Mägi, C.; Fontecha, P.; Manzanares, M. C.; Franch, J.; Ginebra, M. P. Osteogenesis by Foamed and 3D-Printed Nanostructured Calcium Phosphate Scaffolds: Effect of Pore Architecture. *Acta Biomater.* **2018**, 79, 135-147.

(42) Espanol, M.; Perez, R. A.; Montufar, E. B.; Marichal, C.; Sacco, A.; Ginebra, M. P. Intrinsic Porosity of Calcium Phosphate Cements and its Significance for Drug Delivery and Tissue Engineering Applications. *Acta Biomater*. **2009**, 5, 2752-2762.

(43) Montufar, E. B.; Traykova, T.; Gil. C.; Harr, I.; Almirall, A.; Aguirre, A.; Engel, E.; Planell, J. A.; Ginebra, M. P. Foamed Surfactant Solution as a Template for Self-Setting Injectable Hydroxyapatite Scaffolds for Bone Regeneration. *Acta Biomater.* **2010**, 6, 876-885.

(44) National Research Council. *Guide for the Care and Use of Laboratory Animals*; National Academy Press: Washington, DC, 1996; pp 41-194.

(45) Directive 2010/63/EU of the European Parliament and of the Council of 22 September 2010 on the Protection of Animals Used for Scientific Purposes. Available at http://data.europa.eu/eli/dir/2010/63/oj.

(46) Lewin, S.; Barba, A.; Persson, C.; Franch, J.; Ginebra, M. P.; Öhman-Mägi, C. Evaluation of Bone Formation in Calcium Phosphate Scaffolds with μCT – Method Validation Using SEM. *Biomed. Mater.* **2017**, 12, 65005.

(47) LeGeros, R. Z.; LeGeros, J. P.; Trautz, O. R.; Shirra, W. P. Conversion of Monetite, $CaHPO_4$, to Apatites: Effect of Carbonate on the Crystallinity and the Morphology of the Apatite Crystallites. *Adv. X-ray Anal.* **1971**, 14, 57-66.

(48) Berzina-Cimdina, L.; Borodajenko, N. *Research of Calcium Phosphates Using Fourier Transform Infrared Spectroscopy*. In: *Infrared Spectroscopy: Materials Science, Engineering and Technology*; Theophile T., 1st ed; IntechOpen Ltd: London, 2012; pp 123-148.

(49) Wilson, R. M.; Elliott, J. C.; Dowker, S. E. P.; Rodriguez-Lorenzo, L. M. Rietveld Refinements and Spectroscopic Studies of the Structure of Ca-Deficient Apatite. *Biomaterials* **2005**, 26, 1317-1327.

(50) Fleet, M. E. The Carbonate Ion in Hydroxyapatite: Recent X-Ray and Infrared Results. *Front. Biosci. (Elite Ed)* **2013**, 5, 643-652.

(51) Rey, C.; Renugopalakrishnan, V.; Collins, B.; Glimcher, M. J. Fourier Transform Infrared Spectroscopic Study of the Carbonate Ions in Bone Mineral During Aging. *Calcif. Tissue Int.* **1991**, 49, 251-258.

(52) Chan, O.; Coathup, M. J.; Nesbitt, A.; Ho, C. Y.; Hing, K. A.; Buckland, T.; Campion, C.; Blunn, G. W. The Effects Of Microporosity On Osteoinduction Of Calcium Phosphate Bone Graft Substitute Biomaterials. *Acta Biomater.* **2012**, 8, 2788-2794.

(53) Davison, N. L.; Su, J.; Yuan, H.; Van Den Beucken, J. J.; De Bruijn, J. D.; Barrère-De Groot, F. Influence of Surface Microstructure and Chemistry on Osteoinduction and Osteoclastogenesis by Biphasic Calcium Phosphate Discs. *Eur. Cell. Mater.* **2015**, 29, 314-329.

(54) Zhang, J.; Luo, X.; Barbieri, D.; Barradas, A. M. C.; de Bruijn, J. D.; van Blitterswijk, C. A.; Yuan, H. The Size of Surface Microstructures as an Osteogenic Factor in Calcium Phosphate Ceramics. *Acta Biomater*. **2014**, 10, 3254-3263.

(55) Sadowska, J. M.; Guillem-Marti, J.; Montufar, E. B.; Espanol, M.; Ginebra, M. P. Biomimetic Versus Sintered Calcium Phosphates: The In Vitro Behavior of Osteoblasts and Mesenchymal Stem Cells. *Tissue Eng. Part A* **2017**, 23, 1297-1309.

(56) Sadowska, J. M.; Guillem-Marti, J.; Espanol, M.; Stähli, C.; Döbelin, N.; Ginebra, M. P. In Vitro Response of Mesenchymal Stem Cells to Biomimetic Hydroxyapatite Substrates: a New Strategy to Assess the Effect of Ion Exchange. *Acta Biomater*. **2018**, 76, 319-332.

(57) Stein, G. S.; Lian, J. B.; Owen, T. A. Relationship of Cell Growth to the Regulation of Tissue-Specific Gene Expression during Osteoblast Differentiation. *FASEB J*. **1990**, 4, 3111-3123.

(58) Garimella, R.; Tague, S. E.; Zhang, J.; Belibi, F.; Nahar, N.; Sun, B. H.; Insogna, K.; Wang, J.; Anderson, H. C. Expression and Synthesis of Bone Morphogenetic Proteins by Osteoclasts: a Possible Path to Anabolic Bone Remodeling. *J. Histochem. Cytochem.* **2008**, 56, 569-577.

(59) Pederson, L.; Ruan, M.; Westendorf, J. J.; Khosla, S.; Oursler, M. J. Regulation of Bone Formation by Osteoclasts Involves Wnt/BMP Signaling and the Chemokine Sphingosine-1-Phosphate. *Proc. Natl. Acad. Sci. U.S.A* **2008**,105, 20764-20769.

(60) Kreja, L.; Brenner, R. E.; Tautzenberger, A.; Liedert, A.; Friemert, B.; Ehrnthaller, C.; Huber-Lang, M.; Ignatius, A. Non-resorbing Osteoclasts Induce Migration and Osteogenic Differentiation of Mesenchymal Stem Cells. *J. Cell. Biochem.* **2010**, 109, 347-355.

(61) Guihard, P.; Danger, Y.; Brounais, B.; David, E.; Brion, R.; Delecrin, J.; Richards, C. D.; Chevalier, S.; Rédini, F.; Heymann, D.; Gascan, H.; Blanchard, F. Induction of Osteogenesis in Mesenchymal Stem Cells by Activated Monocytes/Macrophages Depends on Oncostatin M Signaling. *Stem Cells* **2012**, 30, 762-772.

(62) Beck Jr, G. R. Inorganic Phosphate as a Signaling Molecule in Osteoblast Differentiation. *J. Cell. Biochem.* **2003**, 90, 234-243.

(63) Dvorak, M. M.; Riccardi, D. Ca^{2+} as an Extracellular Signal in Bone. *Cell Calcium* **2004**, 35, 249-255.

(64) Habibovic, P.; Bassett, D. C.; Doillon, C. J.; Gerard, C.; McKee, M. D.; Barralet, J. E. Collagen Biomineralization in Vivo by Sustained Release of Inorganic Phosphate Ions. *Adv. Mater.* **2010**, 22, 1858-1862.

(65) Barradas, A. M. C.; Fernandes, H. A. M.; Groen, N.; Chai, Y. C.; Schrooten, J.; van de Peppel, J.; van Leeuwen, J. P.; van Blitterswijk, C. A.; de Boer, J. A Calcium-Induced Signaling Cascade Leading to Osteogenic Differentiation of Human Bone Marrow-Derived Mesenchymal Stromal Cells. *Biomaterials* **2012**, 33, 3205-3215.

(66) Ambrosio, L.; Guarino, V.; Sanginario, V.; Torricelli, P.; Fini, M.; Ginebra, M. P.; Planell, J. A.; Giardino, R. Injectable Calcium-Phosphate-Based Composites for Skeletal Bone Treatments. *Biomed. Mater.* **2012,** 7, 024113.

(67) Guo, H.; Su, J.; Wei, J.; Kong, H.; Liu, C. Biocompatibility and Osteogenicity of Degradable Ca-Deficient Hydroxyapatite Scaffolds from Calcium Phosphate Cement for Bone Tissue Engineering. *Acta Biomater*. **2009**, 5, 268-278.

(68) Cuzmar, E.; Perez, R. A.; Manzanares, M. C.; Ginebra, M. P.; Franch, J. In Vivo Osteogenic Potential of Biomimetic Hydroxyapatite/Collagen Microspheres: Comparison with Injectable Cement Pastes. *PLoS One* **2015**, 10, e0131188.

(69) Habibovic, P.; Yuan, H.; van den Doel, M.; Sees, T. M.; van Blitterswijk, C. A.; de Groot, K. Relevance of Osteoinductive Biomaterials in Critical-Sized Orthotopic Defect. *J. Orthop. Res.* **2006**, 24, 867-876.

(70) Yuan, H.; van Blitterswijk, C. A.; de Groot, K.; de Bruijn, J. D. A Comparison of Bone Formation in Biphasic Calcium Phosphate (BCP) and Hydroxyapatite (HA) Implanted in Muscle and Bone of Dogs at Different Time Periods. *J. Biomed. Mater. Res. A* **2006**, 78, 139-147.

Table of Contents/Abstract Graphic